Research Square

Preprints are preliminary reports that have not undergone peer review.
They should not be considered conclusive, used to inform clinical practice,
or referenced by the media as validated information.

Global assessment of marine CO2 removal efficiency in the coastal ocean

Yinghuan Xie

yinghuan.xie@whoi.edu

University of Tasmania https://orcid.org/0000-0001-6809-1920

Paul Spence

Institute for Marine and Antarctic Studies, University of Tasmania, Hobart, Australia.

Stuart Corney

University of Tasmania https://orcid.org/0000-0002-8293-0863

Lennart Bach

University of Tasmania https://orcid.org/0000-0003-0202-3671

Article

Keywords:

Posted Date: October 20th, 2026

DOI: https://doi.org/10.21203/rs.3.rs-11414863/v1

License: This work is licensed under a Creative Commons Attribution 4.0 International License.
Read Full License

Additional Declarations: There is **NO** Competing Interest.

Global assessment of marine CO_2 removal efficiency in the coastal ocean

Yinghuan Xie[1,2], Paul Spence[1,2,3], Stuart Corney[1,2] and Lennart T. Bach[1]

1 Institute for Marine and Antarctic Studies, University of Tasmania, Hobart, Australia

2 Australian Antarctic Partnership Program, University of Tasmania, Hobart, Australia

3 Australian Centres of Excellence for Antarctic Science and Our Future Oceans and 21st Century Weather, University of Tasmania, Hobart, Australia

Corresponding author: Y. Xie (yinghuan.xie@utas.edu.au)

Abstract

Marine carbon dioxide removal (mCDR) removes CO_2 from seawater to enable additional uptake of anthropogenic CO_2 by the ocean. However, this uptake is very slow, limiting mCDR efficiency on years to century timescales. Furthermore, it occurs over vast spatial scales, making estimates with real world measurements unfeasible and robust estimates with conventional ocean models expensive. Here, we develop a novel approach that uses virtual particle tracking of mCDR-perturbed absorbers, which accumulate atmospheric CO_2 along their trajectories. Benchmarking against state-of-the-art ocean model simulations shows that absorbers can reproduce the global structures of mCDR efficiency estimated by a low-resolution (1°) model (±8%) and mCDR efficiency from 12 selected sites estimated with a high-resolution (0.1°) model (±4%), while being 10^2 and 10^6 times computationally cheaper. This advance enabled assessing mCDR efficiency on all coastlines around the world at 4-12 km resolution. This high-resolution global assessment found that 10-year mCDR efficiency was generally high (efficiency>80%) across (sub)tropical coasts, but more limited around Antarctica and parts in the North Atlantic, the Mediterranean, North-East-Asian coastlines, and some Southern Hemisphere mid-latitudes. Furthermore, dense nearshore sampling reveals 30-50% efficiency differences over tens to hundreds of kilometres, showing that coastal mCDR efficiency estimates depend on high-resolution assessments. Through integration into accessible online tools, our study provides a transparent and spatially explicit assessment of where coastal mCDR interventions are most likely to provide efficient atmospheric CO_2 uptake.

Main text

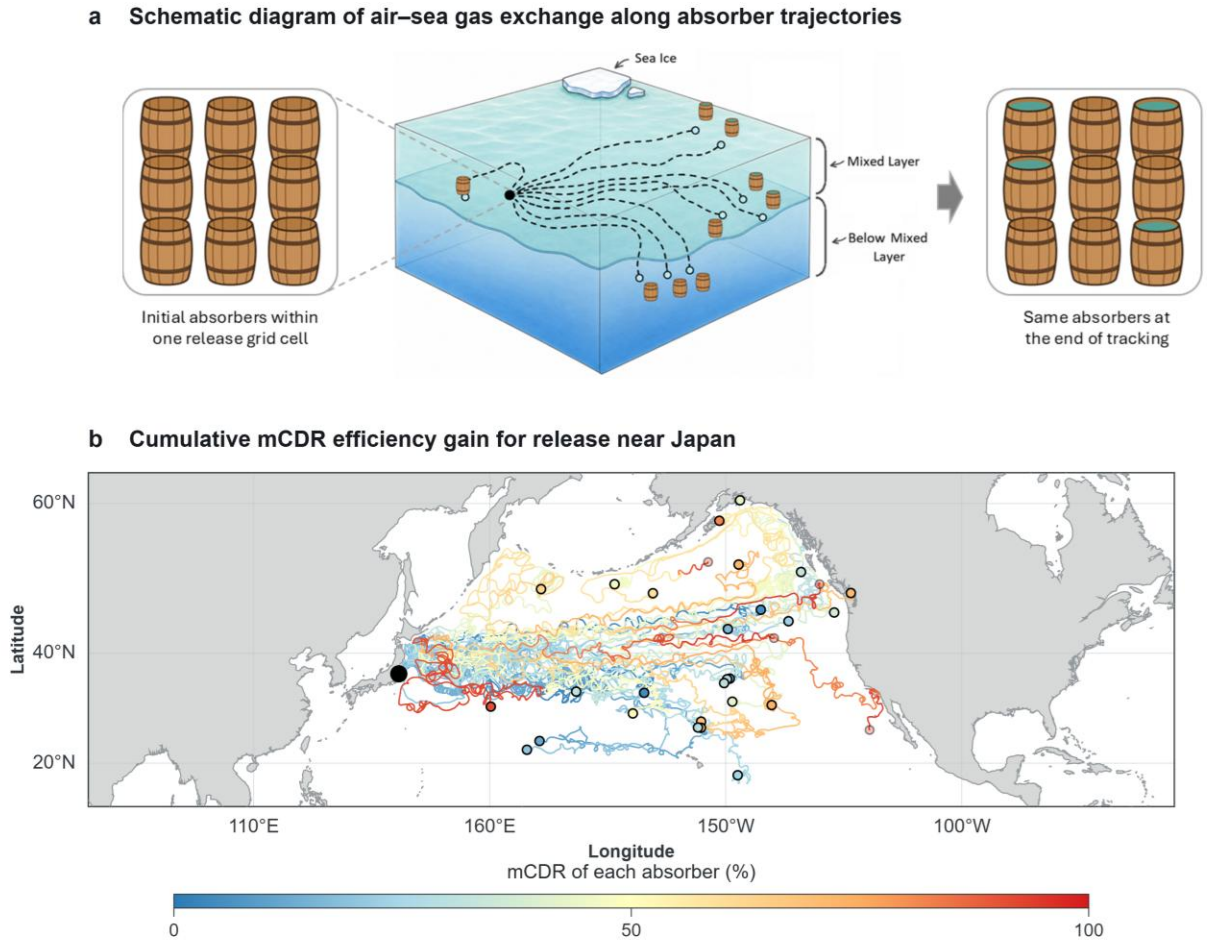
Keeping global warming below 2 °C requires rapid emissions reduction. Additionally, 6-10 Gt CO_2 need to be removed from the atmosphere per year by 2050, using a portfolio of carbon dioxide removal (CDR) methods [1]. Marine CDR (mCDR) methods are considered to be among the most scalable within this CDR portfolio, due to the large size of the ocean and its natural carbon reservoir [2]. However, mCDR methods create a surface-ocean seawater CO_2 deficit that is equilibrated only when atmospheric CO_2 enters the ocean. The rate and extent of this air-sea CO_2 equilibration determine the mCDR efficiency, defined here as the time-dependent equilibration of a seawater CO_2 deficit with atmospheric CO_2. As this equilibration occurs on the ocean basin scale and takes months to decades (or even centuries under some physical regimes), we are unable to continuously monitor mCDR efficiency in the real world. Instead, the assessment of mCDR efficiency critically depends on numerical model simulations [3–8].

Air-sea CO_2 equilibration is controlled by physical and biogeochemical processes. CO_2-deficient water must remain within, or repeatedly return to, the surface layer for air-sea gas exchange to act. The equilibration rate depends on wind speed, sea-ice cover, temperature-dependent gas transfer and carbonate chemistry buffering. Existing (conventional) model experiments have revealed global patterns and seasonal distribution of mCDR equilibration [7–9]. However, the computational cost of such conventional simulations strongly constrains the number of mCDR deployment sites, seasons, parameterizations and resolutions that can be tested. Real-world measurements of equilibration of an mCDR-induced seawater CO_2 deficit will likely be practically impossible in the medium-term, due to the vast spatial-temporal scales over which air-sea CO_2 equilibration occurs [3] (Fig. 1b).

Here, we address this critical limitation by implementing “virtual absorbers” into Lagrangian particle tracking [10], which uses existing physical and biogeochemical fields generated by existing ocean model simulations (Fig. 1). Each absorber represents a fraction of the mCDR perturbation, which is established by assigning absorbers with a deficit in dissolved inorganic carbon (DIC) relative to the surrounding seawater [11]. This DIC deficit causes a CO_2 deficit that decays through air-sea CO_2 exchange. When the absorber is within the mixed layer, the remaining deficit is reduced by a gas-exchange loss term. When it is below the mixed layer, no direct air-sea compensation occurs. The method is modular: Absorber trajectories, gas exchange strength, carbonate sensitivity, sea-ice coverage and mixed-layer exposure are treated explicitly, allowing the method to be used across model products and spatial resolutions. We first benchmarked the method against existing simulations, which had previously assessed mCDR-induced CO_2 equilibration rates with conventional, coarse- and high-resolution global models [7,8,12]. Afterwards, we used virtual absorbers in 0.1° coastal release experiments to study the global coastal structure of mCDR efficiency, as the coastal ocean is where mCDR is expected to occur primarily [9,13,14].

Figure 1: Virtual absorbers for mCDR air-sea equilibration.

a) Virtual absorbers, here illustrated as barrels, are released as an ensemble at a given location. Initially, absorbers share a pre-defined CO_2 deficit relative to the surrounding (barrels are empty; 0% CO_2 uptake). Once released, naturally buoyant absorbers disperse with ocean currents and absorb CO_2 when they in or near the surface layer, until the initial CO_2 deficit is compensated (barrel is full; 100% CO_2 uptake). b) Example ensemble release near Japan, showing CO_2 (percentage) uptake along absorber trajectories (lines) and 5-year final absorber equilibration states (circles).



Results

Benchmarking against conventional modelling

We first tested whether the virtual absorber approach reproduces globally gridded mCDR efficiencies that had previously been estimated with an ocean-sea ice only version of the Community Earth System Model 2 (CESM2) at coarse spatial (1°) and temporal (1 month) resolutions [7,12]. We find that the absorber method reasonably reproduces the main global patterns of mCDR efficiency (Fig. 1a–c). The mean absolute error across all efficiency estimates, pooled over sites and time, is 7.7%, and 97.8% of the 690 site-level comparisons between the absorber method and CESM2 fall within ±30%.

We observed relatively good agreement between the methods in the tropics, although the absorber method underestimates equilibration by ~5% relative to CESM2 when averaged over all tropical sites (Fig. 2d). In the mid-latitudes, the absorber method (on average) initially overestimates equilibration before settling at a ~2% underestimation after 5-7 years. The largest systematic biases occur in high-latitude deep-water formation regions (Fig.2d), and in mid- to high-latitude open-ocean regions. These biases are likely related to the fact that monthly, low-resolution velocity fields cannot fully represent deep-water formation processes, which further leads to a higher mCDR efficiency estimation, as subduction is suppressed.

Next, we compared absorber mCDR efficiencies to simulations with the Australian Community Climate and Earth System Simulator Ocean Model (ACCESS-OM2) [15]. This comparison was conducted across 12 globally representative nearshore regions and at two resolutions [8] : 1° and monthly (ACCESS-OM2) as well as 0.1° and daily resolution (ACCESS-OM2-01). These comparisons show that increasing spatiotemporal resolution substantially increase the agreement in mCDR efficiency between the absorber and the conventional modelling method (Fig. 2e, f). At low resolution, differences initially exceed 20% at some study sites, while settling at a mean absolute error of 8.0% from beginning to year 13 (Fig. 2e). The differences are particularly pronounced at polar sites, where the low resolution velocity fields used for simulating absorber drift cannot accurately resolve polar low-efficiency regions associated with bottom-water formation. This reveals a limitation of the absorber method in polar oceans when used in low resolution models. Nevertheless, the absorber method is able to provide mCDR efficiency estimates that are broadly consistent (year 10 bias < 10%) with conventional modelling in most regions.

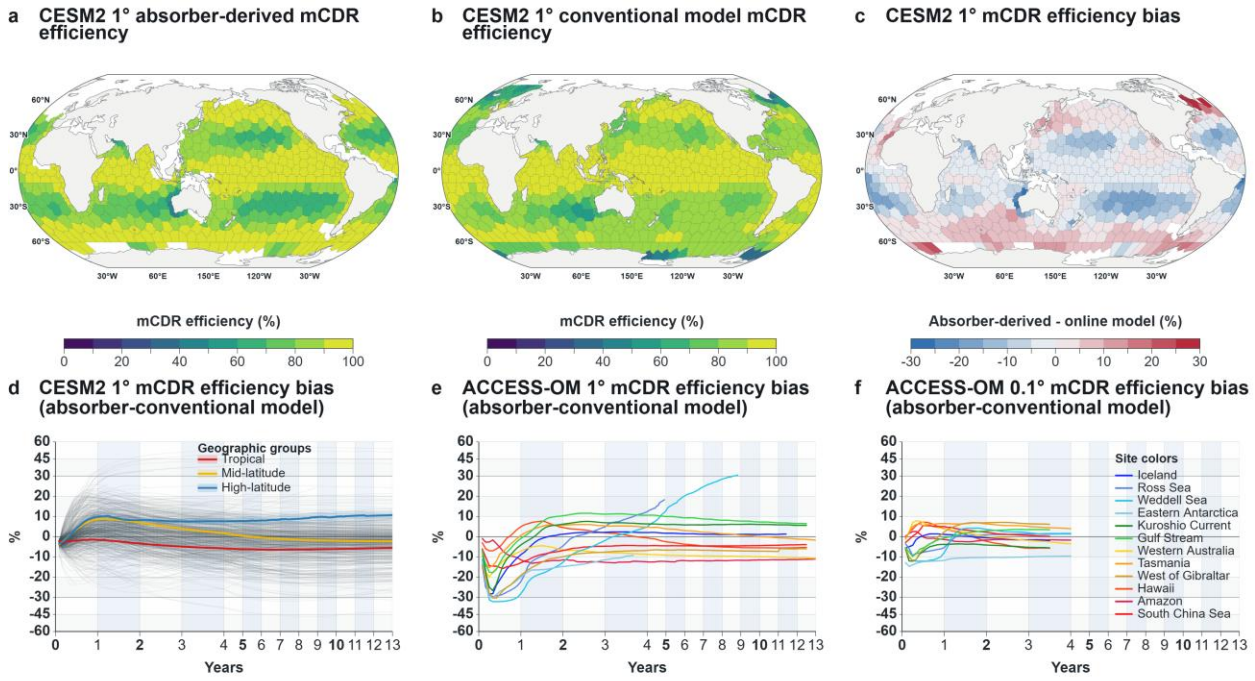
At high model resolution the agreement between the two approaches improves substantially, including in polar sites. During four years of simulation, differences remain more stable, not exceeding 15%, while the mean absolute error is only 4.19% (Fig. 2f).

The computational cost reduction enabled by the absorber method is substantial. Conventional model estimates of mCDR efficiency require hundreds of CPU hours per simulated year at 1° and tens of thousands of CPU hours at 0.1° for each independent mCDR scenario [7,8,15,16]. At market rates, a 10-year simulation for the assessment of a single site costs approximately USD 30–60 at 1° resolution, and USD 30,000–60,000 at 0.1° resolution (see Supplementary Text 1). By using available ocean fields, the absorber method can evaluate many release sites simultaneously, reducing computational cost by roughly two to six orders of magnitude (see Supplementary Text 1, Supplementary Fig. 5). This shifts the

practical question from whether a small number of mCDR scenarios can be simulated to how densely coastlines, seasons and parameter space should be sampled.

Figure 2: Comparing absorber-derived mCDR efficiency with conventional model estimates.

(a-b) mean 10-year mCDR efficiency across 690 sites from the absorber implementation into 1° CESM2 and the conventional online CESM2 estimate from Zhou et al. (2025). Difference in 10-year mCDR efficiency (absorber-method minus online CESM2) shown as gridded dataset (c) and over time (d). In (d), coloured lines indicate the mean for three geographic groups. The bias of each of the 690 curves is shown as a semi-transparent grey line. (e-f) ACCESS-OM2 1° monthly (e) and ACCESS-OM2 0.1° daily (f) absorber simulations compared with conventional estimates at 12 globally distributed reference sites [8]. Note that in (a) and (c-e), for sites with >60% invalid absorber trajectories in later tracking stages, their results were excluded from both figures and statistics (see in Methods).



Global coastal patterns of mCDR efficiency

Using absorbers within the high-resolution model (0.1°) at daily temporal resolution allowed the evaluation of 10-year mCDR efficiencies at 149,521 sites spanning the global coastline south of 75°N. Absorbers were deployed in each of the four seasons (January, April, July and October), leading to 598,084 mCDR efficiency assessments along coastlines. Absorbers were released at the two model grid cells closest to the coast. The spacing between test sites was nominally 0.1°, varying with latitude from approximately 4-12 km.

The 0.1° resolution analysis shows a clear geographic structure in 10-year mCDR efficiency on a global level (Fig. 3a). Tropical and subtropical coasts are generally high-efficiency environments and often approach complete CO_2 equilibration within a decade, for example in the Indo-Pacific, tropical Atlantic, and many low-latitude islands. By contrast, high-latitude Antarctic coastal waters and sea-ice-influenced regions remain low efficiency. Furthermore, larger stretches of lower-efficiency coastlines also occur around Japan, Australia south of 20°S, New Zealand, the Gulf of Oman, the Mediterranean Sea, and some islands in the North Atlantic such as the Canary Islands (Fig. 3a). These regional differences emerge early after absorber initialisation and intensify with time. (Supplementary Fig. 1).

Smaller-scale spatial variability (within ~100 km) in mCDR efficiency between release sites also shows distinguishable geographic features (Fig. 3b). Low-latitude coasts tend to have limited small-scale variability in mCDR efficiency, whereas higher latitudes often show steep gradients within 10s to 100s of kilometres of coastline. Mid-latitude hotspots of local variability occur along the western Pacific margins, the Japanese and East Asian seas, western Europe, the Caribbean and the Mediterranean.

Seasonal variability in mCDR efficiency, which is calculated from the 10-year mCDR efficiency standard derivation of the four experimental seasons, roughly follows the pattern of smaller-scale variability (compare Figs. 3b and 3c). It is concentrated at high latitudes (Fig. 3c), where winter mixed-layer deepening, sea-ice cover, and pronounced seasonal variations in temperature and wind modulate the rate of air–sea gas exchange and the duration for which perturbed waters remain exposed to the atmosphere. Seasonal maps at years 1 and 10 further confirm that the largest monthly contrasts occur in high-latitude regions, whereas low-latitude coasts remain consistently high efficiency across four seasons (Supplementary Fig. 2). Seasonal attribution maps show that the same physical controls recur across seasons, but their relative importance shifts where sea ice and mixed-layer depth vary strongly (Supplementary Fig. 3).

To facilitate detailed access to the underlying data for all 149,521 sites, we developed an interactive data-visualization website as a supplementary resource to this study [17].

Dominant controls of mCDR efficiency

The "dominant attribution analysis" (see Methods) reveals the dominant drivers that shape the spatial patterns in mCDR efficiency (Fig. 3d and Supplementary Fig. 3). We interpreted these patterns using five trajectory-sampled controls on air-sea CO_2 equilibration: mixed-layer residence (whether the absorber is in the mixed-layer or not), sea-ice cover, surface windspeed, carbonate-system sensitivity, and Schmidt-number scaling. Mixed-layer residence and sea-ice cover are first-order control because they regulate the absorber's exposure to the atmosphere. Secondly, surface windspeed regulates gas-transfer intensity following [18,19], carbonate-system sensitivity is represented by β, defined as the ratio of sea-surface $\Delta[CO_2]$ to ΔDIC above the absorber (see methods). A higher β means that a given DIC deficit produces a larger reduction in surface CO_2 concentration, strengthening the air-sea CO_2 gradient and accelerating atmospheric CO_2 uptake. Schmidt-number scaling captures the temperature dependence of CO_2 diffusivity: warm, low-Schmidt-number waters exchange CO_2 more rapidly for a given wind speed, whereas cold, high-Schmidt-number waters slow diffusive exchange.

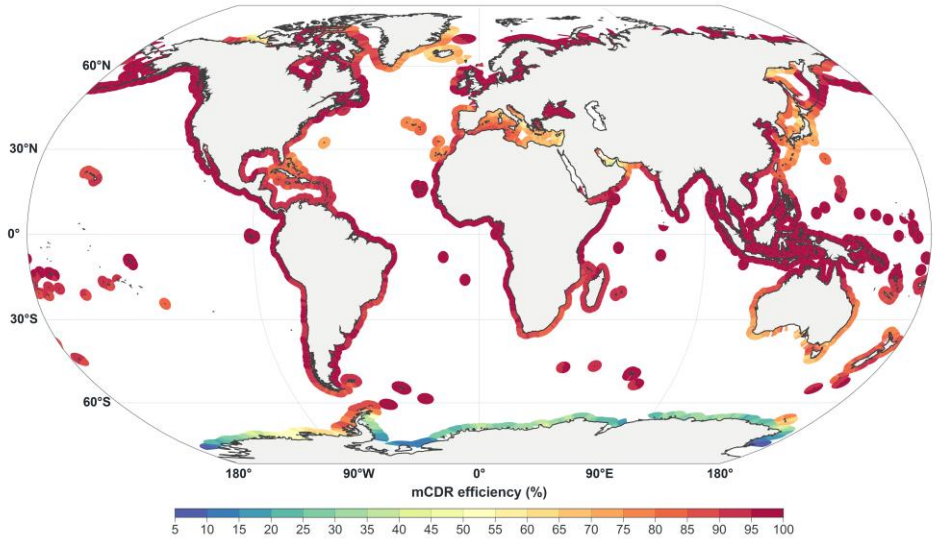
High-efficiency regions (efficiency>90%) are distributed widely in tropical and subtropical coasts, mainly corresponding to environments where absorbers remain in the mixed layer and where gas exchange is accelerated by high β, strong winds or warm water with a low Schmidt number (Fig. 3d).

Low-efficiency regions (efficiency<70%) result from the opposite combination of controls (Fig. 3d). Dominant attribution shows that in most low-efficiency regions the vertical transport moves absorbers out of the mixed layer, carrying the CO_2 deficit into the ocean interior where it cannot be compensated with atmospheric CO_2. Antarctic coastal waters combine several low-efficiency processes: sea-ice cover, cold water, strong seasonal stratification changes and frequent residence below the mixed-layer, producing the lowest 10-year mCDR efficiency globally. Some low-efficiency coastal regions in the North Atlantic (e.g. Greenland) and mid-latitudes (e.g. Hokkaido) similarly reflect efficiency reductions associated with deep mixed layers and/or diapycnal transport from the surface ocean.

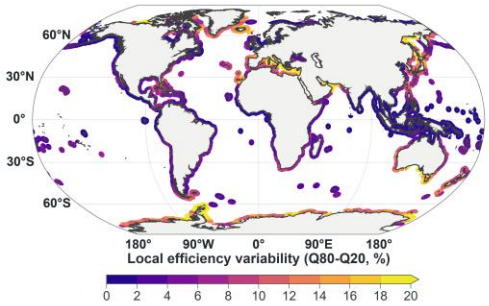
Figure 3: Coastal mCDR efficiency, variability and dominant controls.

(a) Annual mean 10-year coastal mCDR efficiency based on ACCESS-OM2 0.1° daily absorber simulation. Mean values are calculated for 100-km alongshore bins using simulation data from the 149,521 coastal sites across four seasons. For visualization, bin values are extended up to 185 km offshore on the global maps. (b) Spatial variability of 10-year mCDR efficiency around each release site, quantified as the difference between the 80th and 20th percentiles (Q80–Q20) of mCDR efficiency across all sites within a 300 km radius of that release site. Higher values indicate greater local spatial variability in mCDR efficiency. (c) Seasonal standard deviation in 10-year mCDR efficiency, calculated from the mCDR efficiency values of the four experimental seasons at each site. Higher values indicate greater inter-seasonal variability in mCDR efficiency. (d) Dominant drivers of summer 10-year mCDR efficiency across coastlines, using July/January results for the Northern/Southern Hemisphere. Drivers are grouped into three efficiency categories: low efficiency (0–70%; green), intermediate efficiency (70–90%; blue/purple), and high efficiency (90–100%; red/orange/pink). More detailed dominant-driver classifications, including secondary driver combinations, for summer and other seasons are shown in Supplementary Fig. 3.

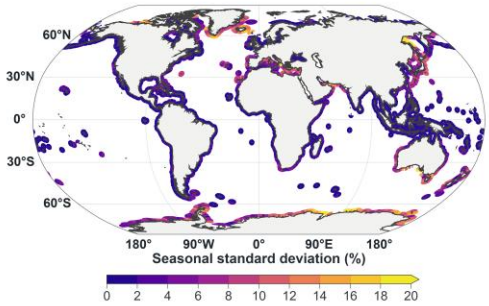
a Four-season mean mCDR efficiency after 10 years of simulation



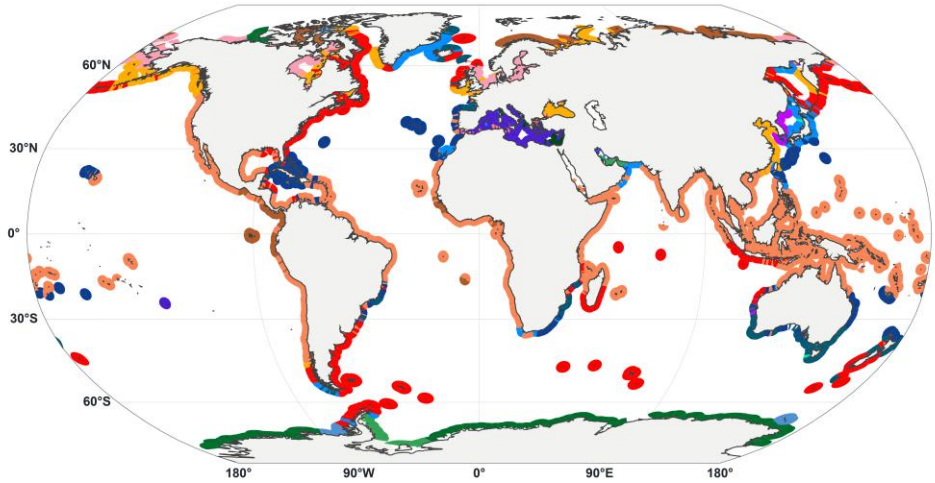
b Spatial variability of mCDR efficiency on small spatial scales.



c Seasonal standard deviation of mCDR efficiency



d Summer (July/January results for Northern/Southern Hemispheres) 10-years mCDR dominant attribution



Dominant attribution per coastal bin:

High-efficiency region classes (mCDR range: 90-100%)
- warm water (low Schmidt number) (23.6%)
- strong wind (high U^2_{10m}) (10.7%)
- high β (6.3%)
- inside ML (6.2%)
- Others and no significant attribution (8.1%)

Middle-efficiency region classes (mCDR range: 70-90%)
- low β (3.7%)
- below ML (3.5%)
- weak wind (low U^2_{10m}) (2.7%)
- strong wind (high U^2_{10m}) (2.3%)
- high sea ice (0.8%)
- Others and no significant attribution (0.6%)

Low-efficiency region classes (mCDR range: 0-70%)
- high sea ice (2.7%)
- below ML (0.9%)
- weak wind (low U^2_{10m}) (0.5%)
- Others and no significant attribution (0.1%)

High resolution reveals nearshore heterogeneity

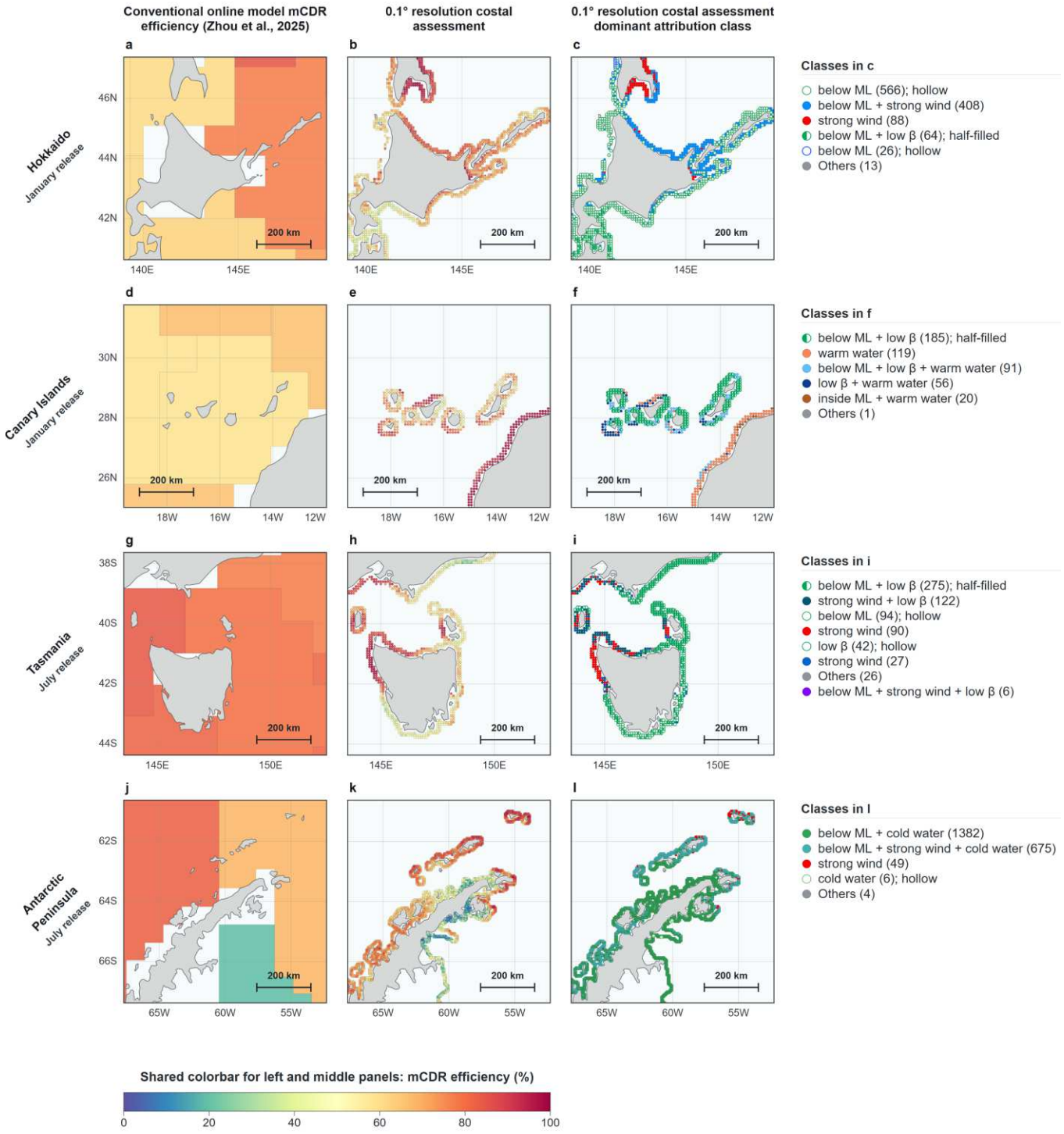
Conventional ocean models are computationally expensive. Therefore, previous studies have estimated mCDR efficiency mostly over relatively coarse spatial resolutions, with individual mCDR deployment regions spanning approximately 2°–20° (100 to 1000s kilometres)[5,7,8,12,20–23]. Fig. 4 reveals that such coarse resolution misses the pronounced gradients that occur along coastlines on short distances. The four locations exemplified in Fig. 4, Hokkaido, the Canary Islands, Tasmania and the Antarctic Peninsula, are hotspots of smaller-scale spatial variability after 10 years of simulation. They show that 10-year mCDR efficiency can vary by roughly 30-50% over tens to hundreds of kilometres. Many contemporary mCDR deployments occur along coasts and on small scales [24,25]. Future mCDR deployments are also expected to remain primarily coastal in due to logistical and regulatory constraints [9,13,14]. Thus, the spatial heterogeneity revealed with absorber simulations represent deployment-relevant coastal features that larger-scale mCDR assessments cannot resolve.

The pronounced small-scale heterogeneity in mCDR efficiency around Hokkaido, the Canary Islands and Tasmania mainly reflect different combinations of below-mixed layer residence, strong-wind exposure and β control while cold water temperature effects play an additional role along the Antarctic Peninsula. Thus, large-scale averaging obscures local variations of mCDR efficiency because it cannot distinguish the relevant local physical and chemical conditions that govern it. For coastal mCDR, the relevant question is not primarily which region is efficient on average, but which nearshore water-mass pathways remain sufficiently exposed to the surface ocean to draw down atmospheric CO_2 over the following decade.

As such, a key finding of this study is that coastal mCDR efficiency cannot be inferred from assessments that average over larger spatial scales. High-resolution simulations show strong regional structure in both the magnitude and drivers of mCDR efficiency. This spatial structure is not noise, it is the oceanographic signal that determines how much atmospheric CO_2 a coastal mCDR intervention can credibly remove over policy-relevant timescales.

Figure 4: Comparison between coarse-resolution and 0.1° resolution assessments of coastal mCDR efficiency and its dominant controls.

(a-c) Hokkaido January release; (d-f) Canary Islands January release; (g-i) Tasmania July release; (j-l) Antarctic Peninsula July release. For each row, the left panels show mCDR efficiency estimated with the conventional modelling approach [7,12] where the simulated mCDR deployment covers very large areas. The middle panels show the 0.1° resolution 10-year coastal absorber assessment for each site. The right panels show dominant attribution classes at the corresponding coastal sites. The left and middle panels share the mCDR efficiency (%) colour scale; numbers in brackets in the legend on the right provide the number of coastal sites that fall into a corresponding attribution class.



Strengths and weaknesses

Estimating mCDR efficiency with the absorber method is one hundred to one million times computationally cheaper than conventional ocean model approaches, while yielding comparable results especially in high-resolution applications (Fig. 2). The method is therefore suitable to generate high-resolution assessments over large spatial scales (Fig. 3, Supplementary Website [17]), which would be prohibitively expensive with conventional modelling methods.

However, the absorber method has other limitations. The framework diagnoses physical and carbonate-chemistry controls on air-sea equilibration, but it is not a coupled Earth-system accounting model. It assumes perturbations remain small enough that background DIC and alkalinity fields provide an adequate carbonate-chemistry reference. It does not represent biological feedbacks, nutrient limitation [26], calcification and dissolution responses [27], atmospheric CO_2 feedbacks [23,28], or local concentration-gradient diffusion from intense deployments [29]. Furthermore, conventional ocean models transport a simulated CO_2 deficit through advective and diffusive processes. Absorbers (which carry the CO_2 deficit) are only displaced through advection, while diffusive processes have to be implemented through a fixed term (horizontally) and simplified parameterization (vertically) (See details in Methods). This limitation makes absorbers physically less representative of water mass dispersal simulated with conventional modelling. Finally, absorbers depend on the ocean current simulations provided by conventional modelling. Thus, the fidelity of the absorber method depends on how well a model outputs (which are used to calculate absorber trajectories) represent ocean currents. Model simulations can insufficiently resolve tidal currents [30], important topographic features [31], or submesoscale transport [32,33], thereby affecting absorber pathways and surface exposure. Meanwhile, because the absorber framework can be readily applied to other models, improved model fidelity should translate directly into improved absorber-based estimates.

These strengths and weaknesses define the appropriate use of the absorber method. It is well suited for high-resolution global screening, model intercomparison, ensemble design, and identifying where and when the much more expensive conventional model simulations are needed most.

Implications

Logistical constraints on infrastructure, energy, and regulation suggest that mCDR will, at least initially, mainly occur along coastlines. Indeed, all mCDR field trials that generate a seawater CO_2 deficit and are documented on an international database are coastal [34]. This coastal concentration makes high-resolution spatial assessment particularly valuable, because deployment feasibility and mCDR efficacy will be sensitive to coastal fine scale variations in bathymetry and circulation.

The geographic structure of mCDR efficiency along coastlines (Fig. 3a) also has direct implications for the implementation of mCDR on the global level. For example, some nations with interest in mCDR like Australia [35], Japan [36], or Saudi Arabia [37] may be geographically disadvantaged, since considerable parts of their coastlines enable comparatively low mCDR efficiency over 10-year timescales. While zooming in reveals that high efficiency hotspots can still be found along these coastlines (from Fig. 3a to Fig. 4b,e,h,k, see Supplementary Website [17]), the overall implication is that mCDR risks significant efficiency losses due to the spatial proximity to low efficiency areas. Importantly, many of the equilibration trajectories at these more critical sites suggest that equilibration stops at lower levels rather than more slowly but continuously increasing over longer timescales. This suggests that the efficiency limitation on mCDR via air-sea CO_2 equilibration extends beyond the 10-year simulations performed herein.

In summary, our new absorber-based approach represents a step towards more efficient and scalable evaluation of mCDR efficiency by providing a robust, yet affordable method for identifying regions of the global ocean where mCDR is most effective. Beyond mapping spatial patterns, the method also enables us to diagnose why some regions exhibit higher efficiencies than others. Importantly, we show that pronounced small-scale variability in mCDR efficiency is a widespread feature, highlighting the need for high-resolution simulations to adequately resolve these variations. Together, these advances provide a stronger basis for assessing and planning coastal mCDR deployment worldwide and are directly supported by an open access online tool [17].

Methods

Absorber experiments

Absorbers are virtual particles that can absorb CO_2 until they are 100% equilibrated with the atmosphere. Absorbers were released at prescribed locations and advected with three-dimensional ocean velocity fields (Table 1) using Ocean Parcels[10]. Absorber positions were recorded with co-located physical and biogeochemical fields, including their own depth, local mixed-layer depth, sea-surface temperature, salinity, sea-ice concentration, background dissolved inorganic carbon, background total alkalinity and 10 m wind speed. The mCDR efficiency was calculated as the mean across absorbers released at the same site and season.

Table 1: Configuration of absorber simulations

Model	1-month mCDR perturbation time	Run length (year)	Velocity field frequency	Model citation
ACCESS-OM2 1°	2004 January/July	13	monthly	Kiss et al. (2020)
ACCESS-OM2 0.1°	2004 January/April/July/October	10	daily	Kiss et al. (2020)
CESM2 1°	1999 January/April/July/October	15	monthly	Danabasoglu et al. (2020)

Mesoscale spreading of absorbers is unresolved in the simulations with monthly 1° fields (ACCESS-OM2, CESM2, see Table 1). In these simulations mesoscale spreading was introduced with a default horizontal diffusivity of 3000 $m^2 \cdot s^{-1}$. For the daily 0.1° ACCESS-OM2 fields, mesoscale structure is partly resolved, and no additional horizontal diffusivity was introduced. When absorbers approach coastlines or the seafloor, advection can occasionally move them into invalid model locations, such as land cells or below the local bathymetry [39,40]. In such cases, the trajectory-tracking routine automatically attempts to relocate the particle to the nearest valid ocean grid point for which velocity fields were available. If this relocation failed, trajectory tracking for that absorber was terminated and it was not considered for the calculation of mCDR efficiency from that point onward.

Vertical exchange within the surface layer was represented by a mixed-layer shuffle that redistributes particles within the mixed layer [39–42]. Specifically, at each 1.5 h time step, absorbers located within the ocean model's mixed layer, were assigned a stochastic vertical displacement within the diagnosed mixed layer. The maximum displacement per time step was 5.4 m (i.e., 0.1cm/s), and the updated particle depth was constrained not to exceed the local mixed-layer depth. This parameterization represents unresolved turbulent stirring in the upper ocean, prevents absorbers from remaining unrealistically fixed at their release depth and preserves the three-dimensional transport resolved by the model velocity fields.

Absorber approach calculation of mCDR efficiency

For each absorber trajectory i and time step t, we first estimate the potential air-sea CO_2 uptake by the absorber that would occur if it was in the mixed layer where CO_2 exchange is possible. This single-step gas-exchange term $K_{i,t}$, is calculated:

$$K_{i,t} = 1 - \exp\left(-0.24 \cdot \frac{G_{i,t}}{h_{absorber}}\right) \text{ (Equation 1)}$$

Here, $G_{i,t}$ is the gas-transfer velocity (described below) and $h_{absorber}$ is the geometric height of the absorber, which is based on absorber's release depth. We used $h_{absorber}$ = 4.6 m for the 1° and 0.1° ACCESS-OM2 simulations, and $h_{absorber}$ = 12 m for CESM2 (Supplementary Text 2). $K_{i,t}$ ranges from 0 to 1, where 0 indicates no atmospheric CO_2 uptake during the time step and 1 indicates that absorbers have taken up all the CO_2 they can at a specific location.

Air-sea exchange is only allowed when the absorber is within the mixed layer. We therefore define a binary exposure term:

$$A_{i,t} = \begin{cases} 1, & Z_{i,t} < ML_{i,t} \\ 0, & Z_{i,t} \geq ML_{i,t} \end{cases} \text{ (Equation 2)}$$

Here, $Z_{i,t}$ is the absorber depth and $ML_{i,t}$ is the mixed-layer depth. Based on sensitivity tests, mixed-layer depth was constrained to 50–1000 m for the 0.1° fields and 100–1000 m for the 1° fields, because these ranges produced absorber-approach estimates most consistent with the conventional model simulations (Supplementary Text 3; Supplementary Fig. 4).

For absorbers within the mixed layer, we define a mixed-layer exposure factor:

$$\Phi_{i,t} = \gamma \frac{h_{absorber}}{ML_{i,t}} \text{ (Equation 3)}$$

$\Phi_{i,t}$ represents the probability of the absorber to be in the surface where air-sea gas exchange can occur, adjusted by the empirical scaling coefficient γ. γ is calibrated against the conventional model approach. We used γ = 1.3 for the 0.1° daily ACCESS-OM2-01 fields, γ = 1.8 for the 1° monthly ACCESS-OM2 fields, and γ = 1.5 for the CESM2 fields (Supplementary Fig. 4). The single-step fractional loss ($L_{i,t}$) of the mCDR perturbation is then calculated as:

$$L_{i,t} = \min(A_{i,t}\Phi_{i,t}K_{i,t}, 1) \text{ (Equation 4)}$$

In most cases, $L_{i,t}$ is less than 1: $A_{i,t}$ and $K_{i,t}$ are both bounded by 1, and $\gamma.h_{absorber}$ is typically smaller than $ML_{i,t}$, so $\Phi_{i,t}$ is also less than 1. If $L_{i,t}$ exceeds 1 in rare cases, we set it to 1, so that the calculated atmospheric CO_2 uptake cannot exceed the maximum capacity of an absorber.

Remaining mCDR perturbation in percentage is accumulated along each trajectory:

$$R_{i,t} = 100\% \prod_{\{t=0\}}^{t}(1 - L_{i,t}) \text{ (Equation 5)}$$

Finally, the cumulative atmospheric CO_2 uptake is calculated as:

$$E_{i,t} = 100\% - R_{i,t} \text{ (Equation 6)}$$

Air-sea gas exchange and carbonate sensitivity

The gas-transfer velocity for the absorbers in ACCESS-OM2 simulations (both 1 and 0.1) was calculated as:

$$G_{i,t} = 0.31\, {U_{i,t}}^2 \left(\frac{Sc(T_{i,t})}{660}\right)^{-\frac{1}{2}} \beta_{i,t} \cdot (1 - fice_{i,t})$$ (Equation 7)

For CESM2 the same equation was used but the gas-transfer coefficient was changed from 0.31 [18] to 0.251 [19] to be consistent with the conventional modelling approach used for CESM2 [7]. In equation 7, $U_{i,t}$ is 10 m wind speed, $T_{i,t}$ is sea-surface temperature, which is approximated by uppermost layer temperature, and $f_ice_{i,t}$ is sea-ice fraction. The Schmidt number Sc is:

$$Sc(T) = 2073.1 - 125.62\, T + 3.6276\, T^2 - 0.043219\, T^3$$ (Equation 8)

Carbonate sensitivity β was estimated with PyCO2SYS [43] as a finite difference in aqueous CO_2 concentration with respect to DIC. Here the ΔDIC is set to 10 mmol m^{-3}:

$$\beta_{i,t} \approx \frac{[\mathrm{CO_2}](\mathrm{DIC}_{i,t}+\Delta\mathrm{DIC},\mathrm{ALK}_{i,t},S_{i,t},T_{i,t}) - [\mathrm{CO_2}](\mathrm{DIC}_{i,t},\mathrm{ALK}_{i,t},S_{i,t},T_{i,t})}{\Delta\mathrm{DIC}}$$ (Equation 9)

Model simulations and absorber release setup

The absorber benchmark experiments used monthly 1° CESM2 simulations for comparison with conventional model estimates of mCDR efficiency [7,12], and ACCESS-OM2 simulations at 1° and 0.1° resolution for comparison with conventional estimates from ACCESS-OM2 [8]. The high resolution coastal mapping experiments used daily ACCESS-OM2 0.1° physical and biogeochemical simulation outputs for 1999-2018, forced by JRA55-do atmospheric fields [44]. Wind fields were taken from three-hourly JRA55-do atmospheric forcing and aggregated to match the temporal resolution of the ocean products.

In the ACCESS-OM2 0.1° absorber experiments, nearshore release locations were defined using the two ocean grid cells closest to the nearest coastline. Absorbers were released for one-month in January, April, July and October 2004. Each monthly release experiment included 149,521 release sites, with one absorber released per site per day, giving 31 absorbers per site in January, July and October, and 30 absorbers per site in April. Because some absorbers can become unintentionally trapped and terminated in complex nearshore topography, we applied a minimum threshold of 6 valid absorbers of the total 30/31 absorbers in each site. Sites below this threshold were excluded from subsequent analyses to retain as much interpretable nearshore mCDR efficiency information as possible while avoiding unstable estimates from very small absorber samples. All data are available through the Supplementary Website [17]. To assess whether 30/31 particles are sufficient to represent the site-level mCDR efficiency, we conducted a series of sensitivity tests. An absorber-number sensitivity test based on 100 randomly selected coastal sites showed that, the 31-absorber configuration retained a 95% confidence-interval half-width within ±5 percentage points in 66 of the 100 coastal sites (Supplementary Fig. 5a). This test therefore shows that 30/31 absorbers are sufficient to obtain robust assessments of mCDR efficiency.

In the absorber vs. Conventional model simulations, absorber releases were strictly co-located with the corresponding conventional model release locations. For the CESM2 1° comparison, absorber particles were released at the 690 sites used in the conventional simulations [7,12]; for the ACCESS-OM2 1° and ACCESS-OM2 0.1° absorber vs. Conventional model comparisons, absorber releases were conducted at the same 12 reference sites used for the conventional simulations [8]. Each site used on the order of 3,000-10,000 absorber particles to minimize stochastic sampling error and ensure robust comparison with the conventional model estimates. Unlike the main coastal experiment, benchmark analyses used a stricter valid-absorber threshold: trapped absorbers were excluded, and sites with <40% valid absorbers were omitted from statistics and figures. Readers can also test the validity threshold to display more or fewer retained results through the Supplementary Website [17].

Accuracy of mCDR efficiency prediction compared with conventional online experiments

Absorber estimates were benchmarked against conventional online model mCDR efficiency by comparing annual efficiency time series and spatial maps at matching sites, release seasons and model products. Difference maps report absorber minus conventional model efficiency (Fig. 2c).

To determine the default empirical scaling coefficient γ values in Eq. 2, we recalculated mCDR efficiency across a range of γ for the ACCESS-OM2 and CESM2 benchmark trajectory ensembles. The results show that γ = 1.3 gives the lowest absorber vs. conventional model prediction error for the 0.1° ACCESS-OM2-01 daily 12-site benchmark, whereas γ = 1.8 and 1.5 provide the more robust low-error configuration for the 1° monthly fields based on the CESM2 690-site four-season benchmark and the ACCESS-OM2 12-site benchmark (Supplementary Fig. 4).

We also tested the sensitivity of the absorber approach to mixed layer depth limits. The sensitivity tests show that the daily 0.1° ACCESS-OM2-01 fields achieved the best agreement between the absorber approach and the conventional model under a 50–1000 m mixed layer depth limit, whereas the 1° ACCESS-OM2 and CESM2 fields showed the closest agreement under a 100–1000 m limit. This difference may reflect the greater ability of the higher resolution and higher frequency ACCESS-OM2-01 fields to represent near-surface water mass transport, allowing shallower absorber trajectories to be assigned exchange weights more realistically. By contrast, the coarser and lower frequency 1° fields may require a stronger shallow mixed layer constraint to avoid assigning unrealistically large exchange weights to shallow trajectories when mesoscale transport is not fully resolved.

Trajectory-based environmental attribution of mCDR efficiency

We used a trajectory-based attribution analysis to identify which environmental conditions were associated with spatial differences in mCDR efficiency. This analysis was descriptive: it tested whether high- and low-efficiency release sites were consistently linked to different air-sea CO_2 exchange environments recorded by the absorber trajectories.

For each release site, site-level environmental descriptors were calculated from all absorbers released at that site. Each site consisted of 30 or 31 absorbers, depending on the release month (see above). Each environmental variable was weighted by the remaining mCDR perturbation, so that conditions recorded

while a larger CO_2 deficit remained had a stronger influence on the site-level descriptor. For an environmental variable X, the trajectory-weighted site mean was calculated as:

$$\bar{X}_S = \frac{\sum_{i=1}^{i=30/31} \sum_t w_{i,t} X_{i,t}}{\sum_{i=1}^{i=30/31} \sum_t w_{i,t}} \text{ (Equation 10)}$$

Here, $X_{i,t}$ is the environmental value (descriptor) sampled by absorber i at time step t, and $w_{i,t}$ is the fraction of the initial mCDR perturbation remaining for that absorber at that time step. The same weighting was applied to sea-ice fraction, wind forcing, Schmidt-number scaling, carbonate sensitivity, and mixed-layer contact.

Different environmental descriptors ($X_{i,t}$) were chosen to represent the main physical and chemical controls on air-sea CO_2 exchange. Sea-ice fraction represents suppression of surface CO_2 exchange. Mixed-layer contact was represented by the binary exposure term ($A_{i,t}$), which indicates whether the absorber was physically connected to the atmosphere. Wind forcing was represented by U^2, which is proportional to the wind contribution to gas transfer. The temperature effect on gas exchange was represented by the Schmidt-number scaling term $Sc_{660}^{-0.5}$, with warmer, lower-Schmidt-number waters corresponding to faster diffusive exchange for the same wind speed. Carbonate sensitivity was represented by β.

To compare descriptors with different units, each site-level descriptor was converted to a standardized anomaly within the same release season:

$$Z_X = \frac{X - \mu_X}{\sigma_X} \text{ (Equation 11)}$$

where μ_X and σ_X are the mean and standard deviation of descriptor X across all valid global sites in that season and window. A positive Z_X therefore indicates that a site sampled more of that environmental condition than the seasonal average.

Sites were grouped into three efficiency regimes using their 10-year mCDR efficiency: high efficiency > 90%, intermediate efficiency 70%–90%, and low efficiency < 70%. We then summarized the dominant environmental features associated with each regime. A descriptor was treated as a primary environmental feature when its signed standardized anomaly was at least 1.0, and as a secondary feature when it was at least 0.5.

For high-efficiency sites, we first tested whether the site had unusually strong mixed-layer contact. If so, the site was classified as mixed layer connected. We then recorded any secondary features associated with enhanced air-sea exchange, including stronger winds, warmer water, or higher carbonate sensitivity. For low-efficiency sites, we first tested whether sea ice was unusually high, because sea ice directly limits surface gas exchange. If sea ice was not the dominant feature, we then tested whether the absorber spent unusually little time in the mixed layer. Other secondary features for low-efficiency sites included weak winds, colder high-Schmidt-number waters, and low carbonate sensitivity. Intermediate-efficiency sites were allowed to include both positive and negative environmental features, reflecting cases where different controls may partly offset each other.

Sites sharing the same efficiency regime and dominant environmental features were grouped into attribution classes. The mean efficiency anomaly, occurrence frequency, and spatial coherence of these classes are summarized in the supplementary webpage (Xie et al., 2026). This analysis identifies environmental conditions that co-vary with spatial patterns in mCDR efficiency along absorber trajectories. It should be interpreted as a descriptive attribution framework, rather than as a single-factor causal perturbation experiment.

Interactive data-visualization tool

To make full use of the absorber method and dataset we build a website [17] that allows users to explore mCDR efficiency at any given coastal site, conduct sensitivity tests, and evaluate the site-specific drivers that explain differences in mCDR efficiency. For any site from any of the four seasonal experiments, users can select the site on the interactive map and move the time slider to visualize the daily trajectories of individual absorbers over the entire 0–10-year period, together with their day-by-day changes in mCDR efficiency. The trajectories are displayed in the map, with an optional depth-based colour scale that allows users to track changes in depth along each trajectory. The website also provides the corresponding daily temporal evolution of wind speed, local mixed-layer depth, background (i.e., excluding the mCDR perturbation) DIC, background total alkalinity, and β for each absorber along its trajectory. The website therefore enables readers to retrieve the complete daily mCDR-efficiency data for any site of interest and to interpret its temporal variability in the context of the evolving physical and chemical conditions encountered by each absorber. This interactive framework was developed to make the large volume of trajectory-resolved model output accessible and interpretable at the individual-site and individual-absorber levels, which cannot be comprehensively represented in figures or tables.

Data availability

The processed data for all main text and supplementary figures are publicly available on Zenodo (https://doi.org/10.5281/zenodo.23073669). Coastal marine CO_2 removal efficiencies and absorber trajectories can also be explored through the supplementary website. The CESM2 model output used in this study is available through the Cworthy DOR Efficiency Atlas on Source Cooperative. The ACCESS-OM2 model fields are held at Australia's National Computational Infrastructure and can be accessed by contacting the corresponding author. The complete particle-trajectory outputs are not included in the Zenodo archive because of their large size but are available from the corresponding author on request.

Code availability

The absorber approach implementation and workflows for ACCESS-OM2-01, ACCESS-OM2-1 and CESM2 are archived on Zenodo (https://doi.org/10.5281/zenodo.23071881). Code for reproducing the main and supplementary figures from the archived data is provided in the figure source-data repository on Zenodo (https://doi.org/10.5281/zenodo.23073669). The underlying ACCESS-OM2 model code is maintained in the COSIMA repository, and the Parcels Lagrangian particle-tracking framework is available from its GitHub repository.

Acknowledgement

We thank Scott Doney and Katrin Meissner for helpful comments on an earlier version of this manuscript. Numerical simulations and data analysis were conducted at the NCI National Facility systems at the Australian National University through the National Computational Merit Allocation Scheme. We thank the Consortium for Ocean–Sea Ice Modelling in Australia (COSIMA). L. T. B. and Y. X. acknowledge funding from the Carbon to Sea Initiative via the Ocean Alk-align project. Y. X. acknowledges support from the China Scholarship Council (202106330008) and the COSIMA consortium. P. S. is supported by ARC grants FT190100413, SR200100008, CE230100012, CE260100001, DP240102358, LP200100406.

References

1. Vaughan, N. *et al.* The State of Carbon Dioxide Removal - 2nd Edition. https://doi.org/10.17605/OSF.IO/F85QJ (2024) doi:10.17605/OSF.IO/F85QJ.
2. Edwards, M. *et al.* The State of Carbon Dioxide Removal - 3rd Edition (2026). https://doi.org/10.17605/OSF.IO/ZRD65 (2026) doi:10.17605/OSF.IO/ZRD65.
3. Bach, L. T., Ho, D. T., Boyd, P. W. & Tyka, M. D. Toward a consensus framework to evaluate air–sea CO_2 equilibration for marine CO_2 removal. *Limnol Oceanogr Letters* lol2.10330 (2023) doi:10.1002/lol2.10330.
4. Fennel, K. *et al.* Modelling considerations for research on ocean alkalinity enhancement (OAE). *State of the Planet* **2-oae2023**, 1–29 (2023).
5. He, J. & Tyka, M. D. Limits and CO_2 equilibration of near-coast alkalinity enhancement. *Biogeosciences* **20**, 27–43 (2023).
6. Ho, D. T. *et al.* Monitoring, reporting, and verification for ocean alkalinity enhancement. *State of the Planet* **2-oae2023**, 1–12 (2023).
7. Zhou, M. *et al.* Mapping the global variation in the efficiency of ocean alkalinity enhancement for carbon dioxide removal. *Nat. Clim. Chang.* https://doi.org/10.1038/s41558-024-02179-9 (2024) doi:10.1038/s41558-024-02179-9.
8. Xie, Y., Spence, P., Corney, S., Tyka, M. D. & Bach, L. T. Effect of Model Resolution on Air-Sea CO2 Equilibration Timescales. *Global Biogeochemical Cycles* **39**, e2024GB008482 (2025).
9. Palmiéri, J. & Yool, A. Global-Scale Evaluation of Coastal Ocean Alkalinity Enhancement in a Fully Coupled Earth System Model. *Earth's Future* **12**, e2023EF004018 (2024).
10. Delandmeter, P. & van Sebille, E. *The Parcels v2.0 Lagrangian Framework: New Field Interpolation Schemes*. https://gmd.copernicus.org/preprints/gmd-2018-339/gmd-2018-339.pdf (2019) doi:10.5194/gmd-2018-339.
11. Bach, L. T. *et al.* Identifying the most (cost-)efficient regions for CO2 removal with Iron Fertilization in the Southern Ocean. *Global Biogeochemical Cycles* **37**, (2023).
12. Chay, F. *et al.* DOR Efficiency - CarbonPlan. *DOR Efficiency - CarbonPlan* https://carbonplan.org/research/dor-efficiency (2025).
13. Lezaun, J. Hugging the Shore: Tackling Marine Carbon Dioxide Removal as a Local Governance Problem. *Front. Clim.* **3**, (2021).
14. Bach, L. T., Vaughan, N. E., Law, C. S. & Williamson, P. Implementation of marine CO2 removal for climate mitigation: The challenges of additionality, predictability, and governability. *Elementa: Science of the Anthropocene* **12**, 00034 (2024).
15. Kiss, A. E. *et al.* ACCESS-OM2 v1.0: a global ocean–sea ice model at three resolutions. *Geosci. Model Dev.* **13**, 401–442 (2020).
16. Colfescu, I. *et al. Porting, Testing, Optimising, and Configuring the Community Earth System Model (CESM2) on ARCHER2*. https://www.archer2.ac.uk/ecse/reports/ARCHER2-eCSE03-06-technical-report.pdf (2022).
17. Xie, Y., Spence, P., Corney, S. & Bach, L. T. Supplementary Website for Global assessment of marine CO2 removal efficiency in the coastal ocean. (2026).
18. Wanninkhof, R. Relationship between wind speed and gas exchange over the ocean. *J. Geophys. Res.* **97**, 7373–7382 (1992).
19. Wanninkhof, R. Relationship between wind speed and gas exchange over the ocean revisited. *Limnology and Oceanography: Methods* **12**, 351–362 (2014).
20. Wang, H. *et al.* Simulated Impact of Ocean Alkalinity Enhancement on Atmospheric CO2 Removal in the Bering Sea. *Earth's Future* **11**, e2022EF002816 (2023).

21. Nuterman, R. & Jochum, M. Impact of marine carbon removal on atmospheric CO2. *Environ. Res. Lett.* **19**, 034011 (2024).
22. Tyka, M. D., Zhou, M., Yankovsky, E. & Carroll, D. Substantial inter-model variation in OAE efficiency between the CESM2/MARBL and ECCO-Darwin ocean biogeochemistry models. *EGUsphere* 1–35 (2025) doi:10.5194/egusphere-2025-3713.
23. Tyka, M. D. Efficiency metrics for ocean alkalinity enhancements under responsive and prescribed atmospheric pCO_2 conditions. *Biogeosciences* **22**, 341–353 (2025).
24. Cyronak, T., Albright, R. & Bach, L. T. Field experiments in ocean alkalinity enhancement research. *State of the Planet* **2-oae2023**, 1–13 (2023).
25. Wynn-Edwards, C. A. *et al.* Alkalinity enhancement with sodium hydroxide in coastal ocean waters. *Sci Rep* **16**, 1842 (2025).
26. Berger, M., Kwiatkowski, L., Bopp, L. & Ho, D. T. Efficacy of seaweed-based carbon dioxide removal reduced by iron limitation and nutrient competition with phytoplankton. *Nat Commun* **17**, 6923 (2026).
27. Bach, L. T., Gill, S. J., Rickaby, R. E. M., Gore, S. & Renforth, P. CO2 Removal With Enhanced Weathering and Ocean Alkalinity Enhancement: Potential Risks and Co-benefits for Marine Pelagic Ecosystems. *Front. Clim.* **1**, 7 (2019).
28. Keller, D. P. *et al.* The Effects of Carbon Dioxide Removal on the Carbon Cycle. *Curr Clim Change Rep* **4**, 250–265 (2018).
29. Anderson, H. J., Mongin, M. & Matear, R. J. Ocean alkalinity enhancement in a coastal channel: simulating localised dispersion, carbon sequestration and ecosystem impact. *Environ. Res. Commun.* **7**, 041012 (2025).
30. Jeon, C.-H. *et al.* Improving surface tidal accuracy through two-way nesting in a global ocean model. *Ocean Modelling* **137**, 98–113 (2019).
31. Kourafalou, V. & Tsiaras, K. A nested circulation model for the North Aegean Sea. *Ocean Science* **3**, 1–16 (2007).
32. Haza, A. C., Özgökmen, T. M., Griffa, A., Garraffo, Z. D. & Piterbarg, L. Parameterization of particle transport at submesoscales in the Gulf Stream region using Lagrangian subgridscale models. *Ocean Modelling* **42**, 31–49 (2012).
33. Verma, V. & Sarkar, S. Lagrangian three-dimensional transport and dispersion by submesoscale currents at an upper-ocean front. *Ocean Modelling* **165**, 101844 (2021).
34. Ocean Visions. Ocean Visions mCDR Field Trial Map. https://oceanvisions.org/mcdr-field-trial-map/.
35. Grant, A. *et al. Australian Carbon Dioxide Removal Roadmap*. https://www.csiro.au/-/media/Science-Connect/Futures/CDR-Roadmap/25-00203_FUT_REPORT_CDRRoadmap_WEB_251106.pdf (2025).
36. Kuwae, T., Watanabe, A., Yoshihara, S., Suehiro, F. & Sugimura, Y. Implementation of blue carbon offset crediting for seagrass meadows, macroalgal beds, and macroalgae farming in Japan. *Marine Policy* **138**, 104996 (2022).
37. Tarbell, B. SWA Partnership: building the model for scalable carbon removal. *Ebb Carbon | SWA Partnership: building the model for scalable carbon removal* https://www.ebbcarbon.com/news/a-new-chapter-how-our-swa-desalination-partnership-creates-a-model-for-scalable-carbon-removal (2025).
38. Danabasoglu, G. *et al.* The Community Earth System Model Version 2 (CESM2). *Journal of Advances in Modeling Earth Systems* **12**, e2019MS001916 (2020).
39. Dawson, H. R. S., Morrison, A. K., England, M. H. & Tamsitt, V. Pathways and Timescales of Connectivity Around the Antarctic Continental Shelf. *JGR Oceans* **128**, (2023).

40. Xie, Y. *et al.* Euphotic Zone Residence Time of Antarctic Bottom Water. *Geophysical Research Letters* **51**, e2023GL106342 (2024).
41. van Sebille, E. *et al.* Abyssal connections of Antarctic Bottom Water in a Southern Ocean State Estimate: AABW PATHWAYS IN SOSE. *Geophys. Res. Lett.* **40**, 2177–2182 (2013).
42. Tamsitt, V., England, M. H., Rintoul, S. R. & Morrison, A. K. Residence Time and Transformation of Warm Circumpolar Deep Water on the Antarctic Continental Shelf. *Geophysical Research Letters* **48**, (2021).
43. Humphreys, M. P., Lewis, E. R., Sharp, J. D. & Pierrot, D. PyCO2SYS v1.8: marine carbonate system calculations in Python. *Geosci. Model Dev.* **15**, 15–43 (2022).
44. Tsujino, H. *et al.* JRA-55 based surface dataset for driving ocean–sea-ice models (JRA55-do). *Ocean Modelling* **130**, 79–139 (2018).
45. Dancheva, T., Alonso, U. & Barton, M. Cloud benchmarking and performance analysis of an HPC application in Amazon EC2. *Cluster Comput* **27**, 2273–2290 (2024).

Supplementary Files

This is a list of supplementary files associated with this preprint. Click to download.

- FigureS1.png
- FigureS2.png
- FigureS3.png
- SupplementaryInformation.docx
- FigureS4.png
- FigureS5.png